

Perturbative calculations of nucleon-deuteron elastic scattering in chiral effective field theory

Lin Zuo,¹ Wendi Chen,² Dan-Yang Pang,³ and Bingwei Long^{1,4,*}

¹*College of Physics, Sichuan University, Chengdu, Sichuan 610065, China*

²*Institute of Applied Physics and Computational Mathematics, Beijing, 100094, China*

³*School of Physics, Beihang University, Beijing, 100191, China*

⁴*Southern Center for Nuclear-Science Theory (SCNT), Institute of Modern Physics, Chinese Academy of Sciences, Huizhou 516000, Guangdong, China*

(Dated: February 9, 2026)

We develop a framework for calculating nucleon-deuteron scattering using strict perturbation theory for treating subleading interactions in chiral effective field theory (ChEFT). Rather than using direct evaluations in the distorted-wave expansion, our approach solves a hierarchy of integral equations to obtain subleading scattering amplitudes. A benchmark with the wave packet continuum-discretization is performed. This framework benefits from the fact that the renormalization-group invariance chiral forces involves only a limited number of two-body partial waves at leading order. We use it to calculate nucleon-deuteron elastic scattering differential cross sections and analyzing powers up to next-to-leading order.

I. INTRODUCTION

The nucleon-deuteron (Nd) system provides an important testing ground for chiral nuclear forces. Not only does it test the prediction of chiral nucleon-nucleon (NN) potentials for the three-nucleon ($3N$) system [1–7], but it also helps understanding the role of $3N$ potentials by quantifying its importance by way of power counting [8–15]. While the bound state of triton and its properties were the natural choice, the scope of investigation is limited by the quantum numbers of the triton state, e.g., the total angular momentum $J = \frac{1}{2}$. Nucleon-deuteron scattering, especially neutron-deuteron scattering, offers more probes to the $3N$ system without having to account for precision-level details of electromagnetic or weak interactions. In recent years, strict perturbative treatment of subleading-order interactions has been increasingly advocated in developing effective field theories (EFTs) for nuclear physics. Perturbation theory on top of a nonperturbative leading-order (LO) has the advantage of disentangling subleading interactions, but it complicates the

* bingwei@scu.edu.cn

computational efforts when the $3N$ continuum problem is already more involved than its bound-state problem. The main focus of this paper is to develop a technique to perform this type of perturbative calculations for chiral nuclear forces in the context of nucleon-deuteron scattering.

As for the nuclear force, we use the power counting developed in Refs. [16–18] to organize chiral NN forces. In constructing the power counting for two-body potentials, these works adopt renormalization-group (RG) invariance as one of the guidelines which requires the phase shifts be independent of the momentum cutoff, an arbitrary parameter of the ultraviolet regularization. The same power counting is examined with the Bayesian analysis for NN scattering data, and it is also employed to study electroweak processes in Refs. [19–21] and triton in Ref. [22]. The one-pion exchange (OPE) potential enters at LO. Therefore, it is the most important long-range nucleon force in chiral EFT and it has a tensor component that behaves like $1/r^3$ at short distances. For attractive singular potentials, such as the OPE tensor force in $^3S_1 - ^3D_1$, 3P_0 , and $^3P_2 - ^3F_2$, etc., RG invariance requires a contact potential, often referred to as a counterterm, to appear at the LO in that partial wave [23–26] even though the naive dimensional analysis (NDA) adopted by Weinberg’s power counting would not [27–29]. Because there are, in principle, an infinite number of attractive singular channels for OPE, one would have to invoke an infinite number of counterterms already at the LO. This conundrum is avoided once we recognize that the OPE does not need to be resummed nonperturbatively in the Lippmann-Schwinger or Schrödinger equation for sufficiently high orbital angular momentum [18, 30] and that the NDA is restored if OPE is treated in pure perturbation theory. We follow Refs. [18] to let OPE enter at the LO only in 1S_0 , $^3S_1 - ^3D_1$, and 3P_0 and at the next-to-leading order (NLO) in all other waves. Not only does this development of two-body chiral forces serve as the foundation of our study of nucleon-deuteron scattering, but it also illustrates the intertwined logic between renormalization, power counting, and perturbation theory for subleading interactions.

A universal feature of the EFTs is the increasing momentum power of higher-order interactions. Although this facilitates expansions for low-momentum initial and final states where momenta Q are much lower than the breakdown scale M_{hi} , these higher-order interactions are not necessarily small for intermediate states with momenta up to the ultraviolet cutoff $\Lambda \gtrsim M_{hi}$. Perturbative renormalization of subleading orders was advocated as a reliable way to ensure that the resulting large contributions from intermediate states can be subtracted by low-energy constants (LECs). Numerous applications of strict perturbation theory in pionless and chiral EFTs can be found in the the recent review in Ref. [31].

A key feature of the power counting of chiral forces used in the paper is that the LO poten-

tials are nonzero only in a limited number of NN partial waves. In the distorted-wave expansion, perturbation theory for subleading potentials is applied by directly evaluating matrix elements between the LO asymptotic states. By contrast, our technique solves a hierarchy of integral equations at subleading orders, all of which share the kernel from the LO equation but have a distinct driving term at each order. This approach of implementing perturbation theory for subleading-order interactions is in line with the method developed in Ref. [32] for the Skorniakov–Ter-Martirosian (STM) equation. A similar framework is developed in Ref. [21] to perturbatively calculate the longitudinal response function of the deuteron.

This paper is organized as the following: in Section II, we describe the numerical framework for solving the Faddeev equation, focusing on the contour-deformation method. In section III, we give details of the perturbative treatment of the NLO potentials. We then present benchmark calculations to validate our methods in Section IV. The LO and NLO results for Nd elastic scattering are presented and discussed in Section V, and we conclude with a summary in Section VI.

II. FADDEEV EQUATION WITH DEFORMED CONTOUR

A. Jacobi partial-wave basis

In our calculations, the Faddeev equation is decomposed in the Jacobi partial-wave basis:

$$|pq\alpha\rangle \equiv |pq (ls)j \left(\lambda \frac{1}{2}\right) IJ \left(t \frac{1}{2}\right) T\rangle. \quad (1)$$

Here, p and q are the magnitudes of the Jacobi momenta: \vec{p} is the relative momentum of the subsystem (nucleons 1 and 2) and \vec{q} is the momentum of the “spectator” (nucleon 3) relative to the center of mass of the subsystem. The quantum numbers l , s , j , and t are, respectively, the orbital angular momentum, spin, total angular momentum, and isospin of the subsystem; λ and I are the orbital angular momentum and total angular momentum of the spectator; and J and T are the total angular momentum and total isospin of the $3N$ system. This paper focuses on Nd elastic scattering, for which $T = \frac{1}{2}$. For simplicity, we use a collective label α to denote these discrete quantum numbers. Our choice for the normalization of the Jacobi partial-wave basis is as follows:

$$\langle p'q'\alpha'|pq\alpha\rangle = \delta_{\alpha'\alpha} \frac{\delta(p' - p)}{p'p} \frac{\delta(q' - q)}{q'q}. \quad (2)$$

We will need the initial and final wave functions $|\phi\rangle$, which describe the configuration in which the nucleon and the deuteron are far apart from each other. To project the initial (or final) wave

function onto the partial-wave basis, we first enumerate all the $3N$ channels that contain a deuteron channel:

$$|\alpha_d\rangle \equiv |(l_d 1) 1 \left(\lambda \frac{1}{2}\right) I J, \left(t \frac{1}{2}\right) \frac{1}{2}\rangle, \quad (3)$$

with $l_d = 0$ or 2 . For a given value of the total $3N$ angular momentum J , there is more than one combination of λI to yield a valid α_d channel. The initial Nd state with definite J , λ , and I is then constructed as

$$|\phi_{\lambda I}^J q_0\rangle = \sum_{l_d=0,2} \int dp p^2 \varphi_{l_d}(p) |pq_0\alpha_d\rangle, \quad (4)$$

where $\varphi_{l_d}(p)$ is the deuteron wave function in the NN partial wave l_d , and q_0 is the center-of-mass momentum of the incoming nucleon.

It is, however, more customary to use the $\lambda\Sigma$ basis to define the phase shifts and mixing angles of Nd elastic scattering, where Σ is the so-called channel spin, i.e., the total spin of the deuteron and the incoming or outgoing nucleon [33]:

$$\vec{\Sigma} = \vec{s}_d + \vec{s}_N. \quad (5)$$

The $\lambda\Sigma$ and the λI bases are related by

$$|\phi_{\lambda\Sigma}^J q_0\rangle = \sum_I (-1)^{J-I} \sqrt{I\Sigma} \left\{ \begin{array}{ccc} \lambda & \frac{1}{2} & I \\ s_d & J & \Sigma \end{array} \right\} |\phi_{\lambda I}^J q_0\rangle. \quad (6)$$

For neutron-deuteron scattering, where the charge of proton does not play a rule, the Faddeev equation can be greatly simplified by assuming the three nucleons are identical fermions. The particle-exchange operators are crucial for implementing this property. If P_{ij} denotes the exchange of the two nucleons labeled by i and j , the $3N$ permutation operator P we need is the sum of the cyclic and anticyclic permutation of the three nucleons:

$$P \equiv P_{12}P_{23} + P_{13}P_{23}. \quad (7)$$

In practical implementation, the permutation operator P is projected onto the Jacobi partial-wave basis (1):

$$\langle p' q' \alpha' | P | pq\alpha \rangle = \delta_{J'J} \delta_{T'T} \int_{-1}^1 dx \frac{\delta(p' - \pi_1)}{p'^{l'+2}} \frac{\delta(p - \pi_2)}{p^{l+2}} G_{\alpha'\alpha}(q'qx), \quad (8)$$

where

$$\pi_1(q', q) = \sqrt{q^2 + \frac{1}{4}q'^2 + xq'q}, \quad (9)$$

$$\pi_2(q', q) = \sqrt{\frac{1}{4}q^2 + q'^2 + xq'q}, \quad (10)$$

and

$$G_{\alpha'\alpha}(q'qx) = \sum_k P_k(x) \sum_{\substack{l'_1+l'_2=l' \\ l_1+l_2=l}} q^{l'_2+l_2} q^{l'_1+l_1} g_{\alpha'\alpha}^{kl'_1l'_2l_1l_2}. \quad (11)$$

Here, the final state quantum numbers such as l', λ', s', \dots , are collectively denoted by α' , and the coefficient $g_{\alpha'\alpha}^{kl'_1l'_2l_1l_2}$ is defined as follows[2]:

$$\begin{aligned} g_{\alpha'\alpha}^{kl'_1l'_2l_1l_2} &= (-) \sqrt{\hat{l}\hat{s}\hat{j}\hat{t}\hat{\lambda}\hat{I}\hat{l}'\hat{s}'\hat{j}'\hat{t}'\hat{\lambda}'\hat{I}'} \left\{ \begin{array}{ccc} \frac{1}{2} & \frac{1}{2} & t' \\ \frac{1}{2} & T & t \end{array} \right\} \sum_{LS} \hat{L}\hat{S} \left\{ \begin{array}{ccc} \frac{1}{2} & \frac{1}{2} & s' \\ \frac{1}{2} & S & s \end{array} \right\} \left\{ \begin{array}{ccc} l & s & j \\ \lambda & \frac{1}{2} & I \\ L & S & J \end{array} \right\} \left\{ \begin{array}{ccc} l' & s' & j' \\ \lambda' & \frac{1}{2} & I' \\ L & S & J \end{array} \right\} \\ &\times \hat{k} \left(\frac{1}{2} \right)^{l'_2+l_1} \sqrt{\frac{(2l+1)!}{(2l_1)!(2l_2)!}} \sqrt{\frac{(2l'+1)!}{(2l'_1)!(2l'_2)!}} \sum_{ff'} \left\{ \begin{array}{ccc} l_1 & l_2 & l \\ \lambda & L & f \end{array} \right\} \left\{ \begin{array}{ccc} l'_2 & l'_1 & l' \\ \lambda' & L & f' \end{array} \right\} C_{l_2\lambda f}^{000} C_{l'_1\lambda' f'}^{000} \\ &\times \left\{ \begin{array}{ccc} f & l_1 & L \\ f' & l'_2 & k \end{array} \right\} C_{kl_1 f'}^{000} C_{kl'_2 f}^{000}. \end{aligned} \quad (12)$$

B. Inhomogeneous Faddeev equation

The inhomogeneous Faddeev equation is diagrammatically demonstrated in Fig. 1. We will use the chiral potentials in our study, and the $3N$ forces do not enter up to NLO, the order we stop at in this paper. Therefore, only two-body potentials are considered here. The yellow blob is the breakup amplitude that starts with an Nd initial state ϕ and ends with three free nucleons in the final state. The solid circle represents the full off-shell, two-body T -matrix, which satisfies the Lippmann-Schwinger equation (LSE)

$$t = V_2 + V_2 G_0 t, \quad (13)$$

where V_2 is the two-body potential and G_0 the free propagator. Denoted by $T|\phi\rangle$, the propagation of the breakup process is given symbolically by the following equation [2, 34]:

$$T|\phi\rangle = tP|\phi\rangle + tPG_0T|\phi\rangle. \quad (14)$$

The total energy of the $3N$ system E_3 is related to the center-of-mass momentum q_0 of the incoming nucleon by

$$E_3 = E_d + \frac{3q_0^2}{4m_N}, \quad (15)$$

where $E_d = -B_d$ is the negative deuteron binding energy.

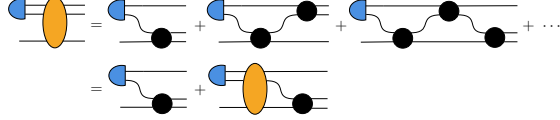


FIG. 1. The diagrammatic representation of the Faddeev equation. The solid line represents the nucleons, the solid circle the two-body off-shell T -matrix, the blue half circle the deuteron, the yellow blob the Faddeev breakup amplitude. Not all the particle-exchange topologies are shown.

The Faddeev equation (14) is solved in the λI basis to obtain the Faddeev breakup amplitude $\langle pq\alpha | T | \phi_{\lambda I}^J \rangle$. In turn, the Nd elastic amplitude U is computed by the following relation[2]:

$$U_{\lambda' \Sigma', \lambda \Sigma}^J(q_0) = \langle \phi_{\lambda' \Sigma'}^J | PG_0^{-1} + PT | \phi_{\lambda \Sigma}^J \rangle , \quad (16)$$

with the basis transformation from λI to $\lambda \Sigma$ carried out according to Eq. (6). The S -matrix of the elastic scattering is directly related to $U_{\lambda' \Sigma', \lambda \Sigma}^J$ by

$$S_{\lambda' \Sigma', \lambda \Sigma}^J(q_0) = \delta_{\lambda' \lambda} \delta_{\Sigma' \Sigma} - i \frac{4\pi}{3} q_0 m_N i^{\lambda' - \lambda} U_{\lambda' \Sigma', \lambda \Sigma}^J . \quad (17)$$

We follow Ref. [33] to parametrize the S -matrix, thereby defining the phase shifts and mixing angles.

C. Deformed Contour

Projecting the abstract operator equations (14), (13) and (16) onto the partial-wave basis yields the integral equations for NN and $3N$ dynamics. The momentum-space integrations in these equations typically contain various singularities. In the numerical computation, we employ contour deformation to circumvent these singularities. Suppose p'' is the integration variable and the original contour runs from 0 to ∞ along the positive real axis, we deform the contour by rotating it clockwise by a small angle θ :

$$p'' = e^{-i\theta} x, \quad x \in \mathbb{R}^+ . \quad (18)$$

In Fig. 2, the rotated contour is illustrated by the ray at the angle θ . For a sufficiently large value of p'' , the deformed contour circles counterclockwise back to $+\infty$ of the real axis. In practical calculations, we always ensure the integrand decays rapidly enough so that the integral along the arc can be neglected. This technique resembles the “complex scaling” method found in many coordinate-space calculations for scatterings and reactions, e.g., in Refs. [35–38].

The implementation begins with the LSE (13):

$$t_{l'\bar{l}'}(p', p, E_2) = V_{l'\bar{l}'}(p', p) + \sum_{\bar{l}'} \int dp'' p''^2 V_{l'\bar{l}'}(p', p'') \frac{t_{\bar{l}l}(p'', p, E_2)}{E_2 - \frac{p''^2}{m_N} + i\epsilon}, \quad (19)$$

where p (p') is the incoming (outgoing) relative momentum and E_2 is the center-of-mass energy of the NN pair. Here we introduce the notation of coupled NN partial waves: $\bar{l} = l$ for uncoupled channels, while for coupled channels, \bar{l} takes the values $j - 1$ and $j + 1$. Not only is the p'' contour deformed by rotation, but the arguments of the full off-shell t -matrix $t(p', p, E_2) — p'$ and p — also take values along the rotated axis. The most obvious singularity is the pole of the free NN propagator at $p'' = \sqrt{m_N E_2}$. The deformed contour clearly avoids it. In our numerical integrations, those “rotated” complex variables are represented by real Gaussian-Legendre mesh points multiplied by a complex phase,

$$p''_n = e^{-i\theta} x_n, \quad (20)$$

so that the integration is approximated by a summation:

$$\int dp'' f(p'') \approx e^{-i\theta} \sum_n w_n f(e^{-i\theta} x_n), \quad (21)$$

where x_n and w_n are the standard abscissas and weights on the positive real axis.

In the ChEFT construction of $V_{l'\bar{l}'}(p', p'')$, the contact potentials are usually polynomials in p' and p'' . Therefore they do not introduce any singularities for the contour integration. But the pion-exchange components of $V_{l'\bar{l}'}(p', p'')$ have nontrivial singularities. The OPE potential $V^{1\pi}$ has the following integral representation in momentum space:

$$V_{l'\bar{l}'}^{1\pi}(p', p'') \propto \int_{-1}^1 dx \frac{P_{l'}(x)}{p'^2 + p''^2 - 2xp'p'' + m_\pi^2}, \quad (22)$$

where $P_l(x)$ are the Legendre polynomials and m_π is the pion mass. For a fixed p' , $V_{l'\bar{l}'}^{1\pi}(p', p'')$ has branch points in the complex p'' -plane at $\pm p' \pm im_\pi$, originating from the end-point singularities of the integral, as illustrated in Fig. (2). As p' varies along the rotated axis, these branch points trace out boundaries that the p'' contour cannot cross, indicated by the solid red lines in the figure. This configuration does not pose a problem because the p'' contour is a ray parallel to these boundaries.

To regularize the ultraviolet behavior of the potential, we apply the following separable regulator:

$$V_{l'\bar{l}'}(p', p) \rightarrow e^{-\frac{p'^4}{\Lambda^4}} V_{l'\bar{l}'}(p', p) e^{-\frac{p^4}{\Lambda^4}}, \quad (23)$$

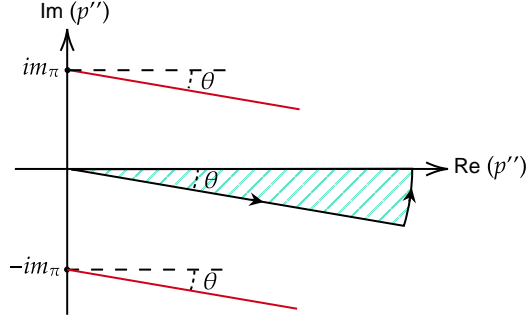


FIG. 2. Diagram showing the analytic structure of $V^{1\pi}(p', p'')$ when the integration contours for both p' and p'' are rotated by an angle θ . The red lines indicate the trajectories of the two branch points at $p'' = p' \pm im_\pi$, which originate from the end-point singularities of the integral.

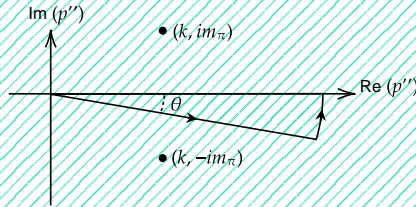


FIG. 3. Analytic structure of $V^{1\pi}(k, p'')$ with the p'' contour rotated by an angle θ . The solid dots points indicate the end-point singularities of the integral.

where Λ is the ultraviolet momentum cutoff. For large p and p' , the regulator has the following asymptotic form:

$$\propto e^{-\cos 4\theta \frac{p^4}{\Lambda^4}} e^{-i \sin 4\theta \frac{p^4}{\Lambda^4}}. \quad (24)$$

The value taken by θ is usually small enough that $\cos 4\theta (p^4/\Lambda^4)$ remains positive, which in turn ensures the proper ultraviolet regularization of $t(p', p, E_2)$.

Although we do not need the on-shell t -matrix $t(k, k, E_2)$ in the paper, where $k = \sqrt{m_N E_2}$ is real, it can be calculated from the off-shell solution by using the known off-shell $t(p'', p, E_2)$ as the input to the right-hand side of Eq. (19). In this contour integration, the branch point $(k, -im_\pi)$ does not cross the deformed contour if $k < m_\pi / \tan \theta$, as illustrated in Fig. 3. This condition imposes an upper limit on the accessible values of k , which is nevertheless sufficiently high for ChEFT applications where on-shell momenta under consideration are normally $\lesssim 3m_\pi$.

The Faddeev equation in momentum space is given by

$$\begin{aligned}
T(p'q'\alpha';\phi) = & \sum_{\bar{\alpha}',l_d} \int_{-1}^1 dx t_{l'\bar{l}'} \left[p', \pi_1(q', q_0), E_3 - \frac{3q'^2}{4m_N} \right] \varphi_{l_d} \left[\pi_2(q', q_0) \right] \frac{G_{\bar{\alpha}'\alpha_d}(q' q_0 x)}{\pi_1^{\bar{l}'}(q', q_0) \pi_2^{l_d}(q', q_0)} \\
& + \sum_{\bar{\alpha}',\alpha''} \int_0^\infty dq'' q''^2 \int_{-1}^1 dx \frac{t_{l'\bar{l}'} \left[p', \pi_1(q', q''), E_3 - \frac{3q'^2}{4m_N} \right]}{E_3 - \frac{q'^2 + q''^2 + xq'q''}{m_N} + i\epsilon} \frac{G_{\bar{\alpha}'\alpha''}(q' q'' x)}{\pi_1^{\bar{l}'}(q', q'') \pi_2^{l''}(q', q'')} \\
& \times T \left[\pi_2(q', q'') q'' \alpha''; \phi \right]. \tag{25}
\end{aligned}$$

Here, $\bar{\alpha}$ denotes the channel coupled to α through the NN interaction, obtained by replacing l in α with \bar{l} . ϕ is the collective symbol for the quantum numbers of the initial state, including q_0 . The integration on the right-hand side of Eq. (25) involves three types of singularities that must be dealt with if all the momenta remain on the real axis, as detailed in Ref. [2]. First, the free propagator G_0 in the q'' integral has a pole if E_3 is above the $3N$ threshold. Second, $t_{l'\bar{l}'}(p', \pi_1, z)$ possesses a branch point at $z = 0$, which is associated with the q' satisfying $E_3 - 3q'^2/(4m_N) = 0$. This induces a singularity of $T(p'q'\alpha';\phi)$ as a function of q' , which in turn produces a singularity of $T(\pi_2 q'' \alpha''; \phi)$ in the q'' integral. Third, in the ${}^3S_1 - {}^3D_1$ channel, $t_{l'\bar{l}'}(p', \pi_1, z)$ has an additional singularity: the deuteron pole at $z = E_d$. If E_3 is above the nucleon-deuteron threshold, the deuteron pole corresponds to a singularity in q' where $E_3 - 3q'^2/(4m_N) = E_d$, which again creates a singularity of $T(\pi_2 q'' \alpha''; \phi)$ in the q'' integral.

In our implementation, these singularities are avoided by letting p' , q' , and q'' in Eq. (25) be rotated complex variables, as defined by Eq. (18), while the on-shell momentum q_0 , the energies E_d and E_3 , and the Legendre variable x remain physical real values. The argument $\pi_2(q', q'')$ of $T(\pi_2 q'' \alpha''; \phi)$ also lies on the rotated contour. Consequently, only one spline operation is required to map $\pi_2(q', q'')$ onto the p'' mesh:

$$T(\pi_2 q'' \alpha''; \phi) \approx \sum_m S_m(|\pi_2|) T(p''_m q'' \alpha''; \phi), \tag{26}$$

where p''_m are the rotated, discrete momenta defined by Eq. (20) and the spline functions S_m are given in Ref. [39]. Using the momentum mesh and Spline functions transforms the integral equation (25) into a linear system, symbolically denoted by

$$\sum_{m n \alpha''} K_{k r \alpha', m n \alpha''} \Psi_{m n \alpha''} = D_{k r \alpha'}, \tag{27}$$

where the indices k , r , m , and n run over the momentum mesh points for p' , q' , p'' , and q'' ,

respectively. The kernel K , the unknown vector Ψ , and the driving term D are defined as follows:

$$K_{kra',mna''} = w_m(p_m'')^2 w_n(q_n'')^2 \langle p_k' q_n' \alpha' | 1 - t P G_0 | p_m'' q_n'' \alpha'' \rangle , \quad (28)$$

$$\Psi_{mna''} = T(p_m'' q_n'' \alpha''; \phi) , \quad (29)$$

$$D_{kra'} = \langle p_k' q_n' \alpha' | t P | \phi \rangle . \quad (30)$$

The Faddeev breakup amplitude T serves as the input for calculating the elastic scattering amplitude U . This procedure is performed by a further integration:

$$\begin{aligned} U_{\lambda' I', \lambda I}^J(q_0) &= \sum_{l_d', l_d} \int_{-1}^1 dx \left(E_3 - \frac{(x+2)q_0^2}{m_N} \right) \frac{\varphi_{l_d'} [\pi_1(q_0, q_0)]}{\pi_1^{l_d'}(q_0, q_0)} \frac{\varphi_{l_d} [\pi_2(q_0, q_0)]}{\pi_2^{l_d}(q_0, q_0)} G_{\alpha_d' \alpha_d}(q_0 q_0 x) \\ &+ \sum_{l_d', \alpha''} \int q''^2 dq'' \int_{-1}^1 dx \frac{\varphi_{l_d'} [\pi_1(q_0, q'')] G_{\alpha_d' \alpha''}(q_0 q'' x)}{\pi_1^{l_d'}(q_0, q'') \pi_2^{l_d''}(q_0, q'')} T [\pi_2(q_0, q'') q'' \alpha''; \phi_{\lambda I}^J] . \end{aligned} \quad (31)$$

$U_{\lambda' I', \lambda I}^J(q_0)$ is then transformed to $U_{\lambda' \Sigma', \lambda \Sigma}^J(q_0)$ via Eq. (6). The integration contour for q'' in Eq. (31) is also rotated, which means that the argument $\pi_2(q_0, q'')$ of T in the second line does not lie on the rotated contour for p' . In order to evaluate $T[\pi_2(q_0, q'') q'' \alpha''; \phi_{\lambda I}^J]$ which is to be fed into Eq. (31), we use again Eq. (25) by setting $p' = \pi_2(q_0, q'')$. Therefore, two additional integration steps are required to compute $U_{\lambda' I', \lambda I}^J(q_0)$ following the initial solution $T(p_n' q_m' \alpha'; \phi)$ solved for via Eq. (25), where p_n' and q_m' are the rotated mesh defined by Eq. (20).

III. PERTURBATION THEORY FOR SUBLEADING ORDER

A key feature of our Faddeev-equation implementation is the perturbative treatment of subleading-order EFT interactions. We adopt the power counting of chiral nuclear forces presented in Refs. [16–18]. At the LO, where the potential must be treated nonperturbatively — that is, where the Faddeev equation, Eq. (25), is solved exactly — we include OPE potentials in the 1S_0 , $^3S_1 - ^3D_1$, and 3P_0 partial waves, in which, contact potentials provide the necessary short-range interactions alongside the OPE. In all other partial waves, OPE is sufficiently weak to be considered as a NLO correction. For 1S_0 and $^3S_1 - ^3D_1$, the contact potential is expressed in momentum space as

$$\langle p'; lsj | V_S^{(0)} | p; lsj \rangle = C_0^{(0)} \quad (32)$$

where the superscript “(0)” indicates LO, and later “(1)” denotes NLO, and so on. We suppress the channel symbol on the LECs when there is no confusion. In 3P_0 , the contact interaction has

Order	NN partial waves
LO	$^1S_0, ^3S_1 - ^3D_1, ^3P_0$
NLO	$^1S_0, ^1P_1, ^3P_1, ^3P_2 - ^3F_2, ^1D_2, ^3D_2, ^3D_3 - ^3G_3$

TABLE I. The NN channels for LO and NLO potentials.

the following form:

$$\langle p'; ^3P_0 | V_S^{(0)} | p; ^3P_0 \rangle = C_0^{(0)} p' p. \quad (33)$$

At NLO, OPE begins to enter other channels, up to the maximum of orbital angular momentum $l \leq 2$. We also keep the higher waves that are coupled to these channels; therefore, $^3P_2 - ^3F_2$ and $^3D_3 - ^3G_3$ are included. In addition, the 1S_0 potential has the following correction at NLO [17]:

$$\langle p'; ^1S_0 | V_S^{(1)} | p; ^1S_0 \rangle = C_0^{(1)} + \frac{D_0^{(1)}}{2} (p'^2 + p^2), \quad (34)$$

where $C_0^{(1)}$ is the NLO correction to the LO LEC $C_0^{(0)}$ and $D_0^{(1)}$ is the LEC associated with the momentum-dependent 1S_0 contact interaction.

A crucial feature of this power counting for implementing the Faddeev equation is the significantly smaller number of channels at LO compared to subleading orders. We leverage this feature to implement a perturbative treatment of the subleading interactions. To this end, the whole space of $3N$ channels \mathcal{C} is decomposed into two sets. The first, \mathcal{A} , consists of Jacobi partial waves whose two-body subsystem is acted upon by the LO interactions, $^1S_0, ^3S_1 - ^3D_1$, and 3P_0 . The remaining channels form the complementary set \mathcal{B} :

$$\mathcal{C} = \mathcal{A} \oplus \mathcal{B}. \quad (35)$$

For a channel β in \mathcal{B} and any other $3N$ channel γ , we have

$$\langle p' q' \beta | V^{(0)} | p q \gamma \rangle = 0. \quad (36)$$

We will see shortly how this seemingly trivial identity facilitates perturbative calculations.

To treat the NLO potential in perturbation theory, we begin with the formal EFT expansion of the two-body potential V , two-body t -matrix t , the three-body Faddeev breakup operator T , and

the initial state ϕ :

$$V = V^{(0)} + V^{(1)} + \dots, \quad (37)$$

$$t = t^{(0)} + t^{(1)} + \dots, \quad (38)$$

$$T = T^{(0)} + T^{(1)} + \dots, \quad (39)$$

$$\phi = \phi^{(0)} + \phi^{(1)} + \dots. \quad (40)$$

These expansions are inserted into Eqs. (13) and (14), yielding the following perturbative hierarchy:

$$T^{(0)} |\phi^{(0)}\rangle = t^{(0)} P |\phi^{(0)}\rangle + t^{(0)} P G_0 T^{(0)} |\phi^{(0)}\rangle, \quad (41)$$

$$T^{(0)} |\phi^{(1)}\rangle = t^{(0)} P |\phi^{(1)}\rangle + t^{(0)} P G_0 T^{(0)} |\phi^{(1)}\rangle, \quad (42)$$

$$T^{(1)} |\phi^{(0)}\rangle = t^{(1)} P |\phi^{(0)}\rangle + t^{(1)} P G_0 T^{(0)} |\phi^{(0)}\rangle + t^{(0)} P G_0 T^{(1)} |\phi^{(0)}\rangle, \quad (43)$$

where the $t^{(1)}$ is given by

$$t^{(1)} = V^{(1)} + V^{(1)} G_0 t^{(0)} + V^{(0)} G_0 t^{(1)}. \quad (44)$$

This is to be compared with the direct calculation of $T^{(1)}$

$$T^{(1)} |\phi^{(0)}\rangle = (1 + T^{(0)} G_0) t^{(1)} P (1 + G_0 T^{(0)}) |\phi^{(0)}\rangle. \quad (45)$$

Equations (41), (42), and (43) share a common integral kernel,

$$K \equiv 1 - t^{(0)} P G_0, \quad (46)$$

but differ in their driving terms,

$$D^{(0)} \equiv t^{(0)} P |\phi^{(0)}\rangle, \quad (47)$$

$$D^{(0,1)} \equiv t^{(0)} P |\phi^{(1)}\rangle, \quad (48)$$

$$D^{(1,0)} \equiv t^{(1)} P (1 + G_0 T^{(0)}) |\phi^{(0)}\rangle. \quad (49)$$

Because of Eq. (36), the operator $t^{(0)} P G_0$ produces the zero vector when acting from the right on a $3N$ channel β from \mathcal{B} :

$$\langle p' q' \beta | t^{(0)} P G_0 | p q \alpha \rangle = 0. \quad (50)$$

As a result, the kernel exhibits a block-triangular structure:

$$K = \begin{pmatrix} K_A & K_{AB} \\ \mathbf{0} & \mathbf{1} \end{pmatrix} \quad (51)$$

where K_A acts only within \mathcal{A} and K_{AB} couples \mathcal{A} to \mathcal{B} :

$$K_A(\alpha', \alpha) = \langle \alpha' | K | \alpha \rangle \quad \alpha, \alpha' \in \mathcal{A}, \quad (52)$$

$$K_{AB}(\alpha', \beta) = \langle \alpha' | K | \beta \rangle \quad \beta \in \mathcal{B}. \quad (53)$$

Here and later when it does not lead to confusion, we omit the labels for the momentum mesh. Upon discretization, K_A is normally a smaller matrix than the full K , therefore saving the computing resources. Accordingly, the unknown vector Ψ and the driving term D are split into two parts as well:

$$\Psi^T = (\Psi_A, \Psi_B), \quad (54)$$

$$D^T = (D_A, D_B), \quad (55)$$

where the unknown vectors for each order are defined as follows

$$\Psi^{(0)} \equiv T^{(0)} |\phi^{(0)}\rangle, \quad (56)$$

$$\Psi^{(0,1)} \equiv T^{(0)} |\phi^{(1)}\rangle, \quad (57)$$

$$\Psi^{(1,0)} \equiv T^{(1)} |\phi^{(0)}\rangle. \quad (58)$$

With this decomposition, we can write Eqs.(41) and (42) as

$$\begin{cases} K_A \Psi_A^{(0)} = D_A^{(0)}, \\ \Psi_B^{(0)} = D_B^{(0)} = 0. \end{cases} \quad (59)$$

and

$$\begin{cases} K_A \Psi_A^{(0,1)} = D_A^{(0,1)}, \\ \Psi_B^{(0,1)} = D_B^{(0,1)} = 0. \end{cases} \quad (60)$$

The case of Eq. (43) is more nontrivial

$$\begin{cases} K_A \Psi_A^{(1,0)} = D_A^{(1,0)} - K_{AB} D_B^{(1,0)}, \\ \Psi_B^{(1,0)} = D_B^{(1,0)}, \end{cases} \quad (61)$$

where for $\alpha' \in \mathcal{A}$,

$$D_A^{(1,0)}(\alpha') = \langle \alpha' | t^{(1)} P \left(1 + G_0 T^{(0)} \right) | \phi^{(0)} \rangle, \quad (62)$$

$$K_{AB} D_B^{(1,0)}(\alpha') = - \sum_{\beta \in \mathcal{B}} \langle \alpha' | t^{(0)} P G_0 | \beta \rangle \langle \beta | t^{(1)} P \left(1 + G_0 T^{(0)} \right) | \phi^{(0)} \rangle. \quad (63)$$

Therefore, we are dealing with a linear system that spans only \mathcal{A} even at NLO. While the integral kernel remains identical to that of LO, the main computational efforts at NLO shifts to constructing the driving term. By mathematical induction, one finds that at all higher orders the same kernel is always reused, although with increasingly complex driving terms. Because of this feature, we refer to this approach of perturbative calculations as the fixed-kernel perturbation theory (FKPT) method.

Using $T^{(0)} |\phi^{(0)}\rangle$, $T^{(0)} |\phi^{(1)}\rangle$, and $T^{(1)} |\phi^{(0)}\rangle$ as the inputs, we can express the elastic scattering amplitude at LO and NLO as

$$U^{(0)} = \langle \phi'^{(0)} | PG_0^{-1} + PT^{(0)} | \phi^{(0)} \rangle, \quad (64)$$

$$U^{(1)} = \langle \phi'^{(1)} | PG_0^{-1} + PT^{(0)} | \phi^{(0)} \rangle + \langle \phi'^{(0)} | PT^{(1)} | \phi^{(0)} \rangle + \langle \phi'^{(0)} | PG_0^{-1} + PT^{(0)} | \phi^{(1)} \rangle. \quad (65)$$

In the chiral power counting adopted in this work, the $^3S_1 - ^3D_1$ interaction vanishes at NLO, as noted in Table I. As a result, the NLO correction to the deuteron wave function is also zero, from which we derive that the NLO correction to the initial and final Nd state vanish too:

$$|\phi^{(1)}\rangle = 0. \quad (66)$$

IV. BENCHMARKS

To benchmark our contour-deformation implementation of the Faddeev equation, we compare our results with those obtained from the wave-packet continuum-discretization (WPCD) method [40]. We note other works where the WPCD is successfully combined with different interactions to calculate Nd scattering [10, 41, 42]. For the interaction, we choose the LO potentials with a cutoff value $\Lambda = 400$ MeV in 1S_0 and $^3S_1 - ^3D_1$, that is, using the chiral LO potentials listed in Table I but turning off the 3P_0 component, for technical simplicity. In the deformed-contour calculations, we use 48 mesh points, contour-rotation angle of 10° .

The phase shifts and mixing angles at nucleon laboratory energies $E_N = 3$, 14, and 30 MeV are calculated for $J^P = \frac{1}{2}^\pm$ and $\frac{3}{2}^+$. The results from the two methods are compared in Table II for $J^P = \frac{1}{2}^\pm$ and Table III for $J^P = \frac{3}{2}^+$. Overall, the discrepancies between results of these two methods are less than one percent. Such a level of agreement is sufficient for this study, as the subsequent NLO corrections and cutoff variations will be substantially larger than such differences introduced by different numerical methods.

We also compare the differential cross sections and the nucleon analyzing powers A_y calculated with the two methods, as shown in Fig. 4. Reference [2] is followed to relate the partial-wave

E_N	3 MeV	14 MeV	30 MeV
$^2D_{\frac{1}{2}}$	(-3.37, 0.00)	(-8.43, 0.47)	(-11.03, 1.79)
	(-3.35, 0.00)	(-8.44, 0.47)	(-11.03, 1.79)
$^2S_{\frac{1}{2}}$	(-12.63, 0.00)	(-41.01, 21.88)	(-86.11, 42.16)
	(-12.89, 0.00)	(-41.17, 21.98)	(-86.38, 41.62)
$\eta_{\frac{1}{2}}$	(8.29, 0.00)	(5.73, -0.49)	(6.62, -1.61)
	(8.00, 0.00)	(5.71, -0.49)	(6.61, -1.59)
$^2P_{\frac{1}{2}}$	(-6.00, 0.00)	(7.92, 7.64)	(39.46, 13.71)
	(-5.99, 0.00)	(7.98, 7.63)	(39.76, 13.88)
$^4P_{\frac{1}{2}}$	(16.53, 0.00)	(24.43, 7.51)	(9.17, 5.66)
	(16.50, 0.00)	(24.40, 7.60)	(9.21, 5.70)
$\epsilon_{\frac{1}{2}}$	(4.13, 0.00)	(35.55, 19.30)	(-34.97, 8.80)
	(4.13, 0.00)	(35.85, 19.38)	(-34.78, 8.80)

TABLE II. Phase shifts and mixing angle for $J^P = \frac{1}{2}^\pm$ at different neutron incident energies E_N . For each channel, the results shown in the upper rows are obtained by the contour-deformation method, and those in the lower rows are results calculated with the WPCD method.

amplitude U^J to these observables. For these observables, the partial-wave sum for the scattering amplitude U^J includes contributions up to $J^P \leq \frac{15}{2}^\pm$. The level of agreement on the observables is consistent with that found for the phase shifts in Tables II and III.

Implementing the FKPT method — our perturbative treatment of NLO potentials outlined in Sec. III — requires substantial additions to the code beyond the regular Faddeev-equation solver. To test this functionality, we note that perturbation theory can be implemented straightforwardly with the nonperturbative framework, although at additional computational cost. Starting with an auxiliary potential,

$$V(x) = V^{(0)} + xV^{(1)}, \quad (67)$$

where x is the auxiliary multiplier, we can use the nonperturbative solver, i.e., Eqs. (25) and (31), to calculate the x -dependent scattering amplitude $U(E_3, x)$ for any value of x . By numerically

E_N	3 MeV	14 MeV	30 MeV
$^4S_{\frac{3}{2}}$	(-66.84, 0.00)	(-101.57, 0.82)	(-120.31, 3.57)
	(-66.84, 0.00)	(-101.34, 0.71)	(-119.69, 3.40)
$^2D_{\frac{3}{2}}$	(2.13, 0.00)	(5.67, 1.41)	(6.95, 3.23)
	(2.12, 0.00)	(5.68, 1.42)	(6.96, 3.25)
$^4D_{\frac{3}{2}}$	(-3.82, 0.00)	(-8.22, 0.54)	(-8.17, 1.84)
	(-3.79, 0.00)	(-8.22, 0.54)	(-8.18, 1.84)
$\epsilon_{\frac{3}{2}}$	(1.21, 0.00)	(2.65, -0.34)	(3.21, -0.80)
	(1.22, 0.00)	(2.65, -0.34)	(3.21, -0.81)
$\xi_{\frac{3}{2}}$	(1.34, 0.00)	(3.92, -0.02)	(6.35, -0.15)
	(1.34, 0.00)	(3.92, -0.02)	(6.36, -0.16)
$\eta_{\frac{3}{2}}$	(-0.27, 0.00)	(-0.97, -0.45)	(-1.08, -1.25)
	(-0.27, 0.00)	(-0.97, -0.45)	(-1.09, -1.24)

TABLE III. Phase shifts and mixing angle comparison for $J^P = \frac{3}{2}^+$ at various E_N . For each channel, the results shown in the upper rows are obtained by the contour-deformation method, and those in the lower rows are calculated with the WPCD method.

expanding $U(E_3, x)$ around $x = 0$, we can obtain the NLO scattering amplitude in perturbative theory:

$$U(E_3, x) = U^{(0)}(E_3) + xU^{(1)}(E_3) + \dots \quad (68)$$

This approach is computationally demanding, as it requires performing multiple evaluations of the amplitude at different values of x to perform the Taylor expansion numerically. Furthermore, this auxiliary-potential method has a large memory footprint because it does not account for the significantly smaller size of the LO kernel. While useful for benchmarking, the auxiliary-potential method's limitations justify the implementation of the FKPT approach. For the phase shifts sampled, the two approaches produce consistent results, with at least six identical significant digits.

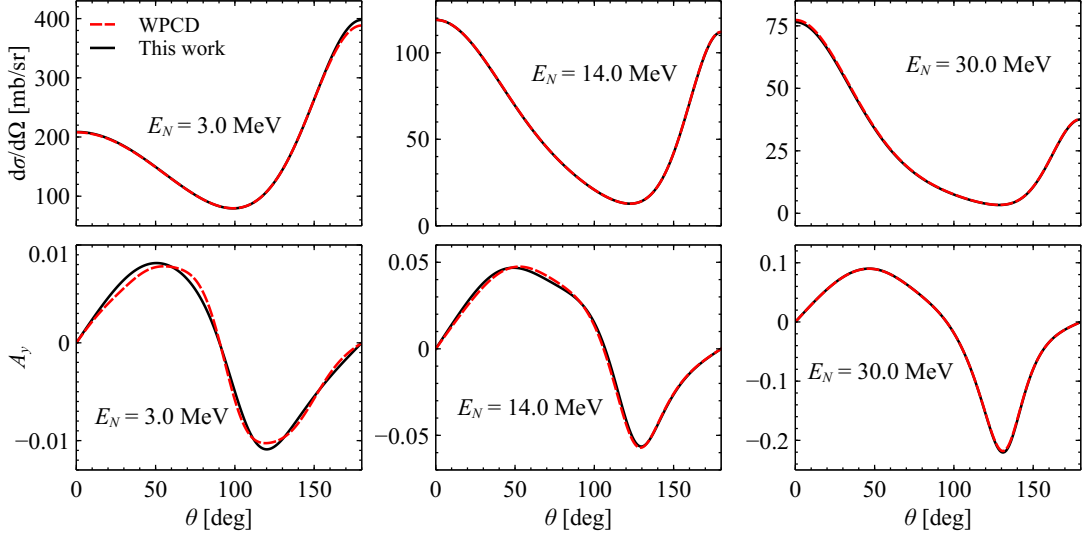


FIG. 4. Comparison of the nd elastic scattering differential cross sections and neutron analyzing powers. Results obtained with the contour-deformation and the WPCD method are shown as solid and dashed curves, respectively.

V. RESULTS

We would like to use Nd elastic scattering to investigate two aspects of the power counting of chiral nuclear forces adopted in the paper. One is the ultraviolet cutoff dependence of the phase shifts, and the other is the effects of the NLO correction. The ultraviolet cutoff Λ introduced in Eq. (23) is arbitrarily chosen, any observables must be independent of its value up to the EFT uncertainty allowed at the given order, a manifestation of the principle of RG invariance. A violation of RG invariance can be interpreted as a defect in the power counting, which can be remedied by promoting certain operators to lower orders. In Ref. [43], RG invariance of the triton binding energy and Nd scattering scattering lengths was observed, resulting in the conclusion that the $3N$ forces are not required up to NLO for renormalization purpose.

We verify this conclusion by inspecting how the phase shifts vary against Λ . Because ultraviolet divergence tends to be suppressed by orbital momenta, it suffices to study the S -wave phase shifts of Nd scattering. When Λ moves above ~ 600 MeV in 3P_0 and above ~ 1000 MeV in $^3S_1 - ^3D_1$, spurious NN bound states start to develop [25]. In order to avoid unphysical breakup thresholds for the Nd system, we remove these spurious states using a method similar to what is described in Ref. [25]. Figure 5 shows the phase shifts of $^2S_{\frac{1}{2}}$ and $^4S_{\frac{3}{2}}$ with Λ varied from 400 to 1600 MeV. Up to $E_N = 108$ MeV, we can see that the phase shifts are converging with respect to Λ .

The angular distributions of the differential cross sections and the nucleon analyzing power A_y

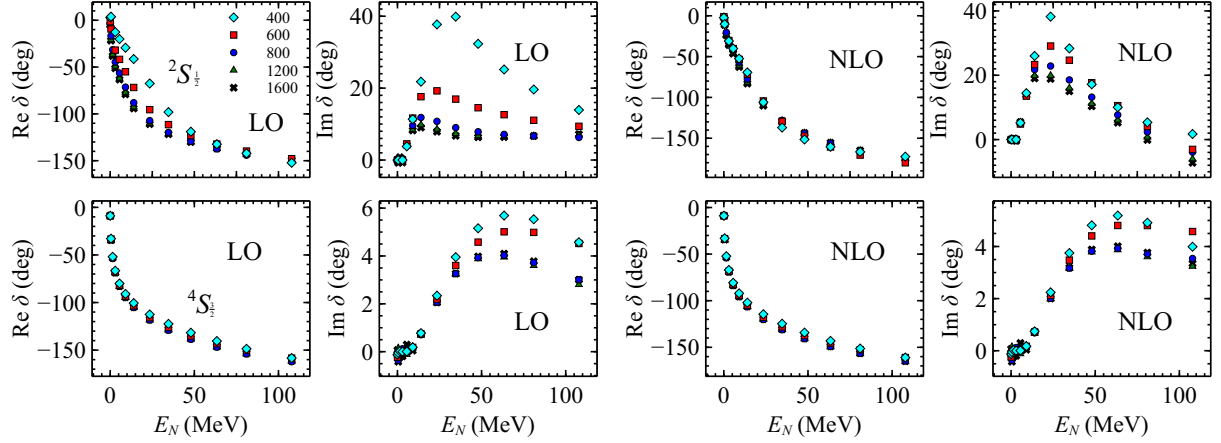


FIG. 5. The doublet and quadruplet S -wave phase shifts as functions of E_N for various cutoff Λ . Top and bottom panels correspond to the $^2S_{\frac{1}{2}}$ and $^4S_{\frac{3}{2}}$ channels, respectively.

are computed to study how much the NLO corrections change relative to LO. These observables are computed with the partial-wave sum truncated beyond $J^P = \frac{19}{2}^+$, at which point including higher waves alters the results by less than 1%. Using $\Lambda = 800$ MeV, Figs. 6 and 7 compare the LO and NLO EFT predictions with available experimental data for these observables at their respective energies. For the angular distribution, we find the LO results agree with the data better than the NLO ones at forward angles. This discrepancy between the NLO and the data is almost entirely driven by repulsion in the 3P_1 channel, which consists of only the OPE potential at the NLO. As shown in Fig. 8, removing the 3P_1 component from the NLO potentials results in the angular distributions nearly identical to the LO results. Using the nucleon-delta mass splitting $\delta = 293$ MeV as the breakdown scale for our delta-less chiral forces, we estimate the EFT expansion error by powers of q_0/δ . For instance, the EFT error for NLO is $(q_0/\delta)^2 \simeq 9\%$ at $E_N = 9.0$ MeV, which is able to explain the discrepancy between the EFT predictions and the data. The LO, however, agrees worse than the NLO with data in terms of describing spin observables. In Fig. 7, the maximum of A_y at LO has the opposite sign relative the experimental data. Due to the lack of nd experimental data, we use pd data in Fig. 7 at $E_N = 35$ MeV. The NLO corrections turn around the wrong trend and are headed to the data. This observation reminds us the delicate nature of spin observables which can only be described well at quite high orders.

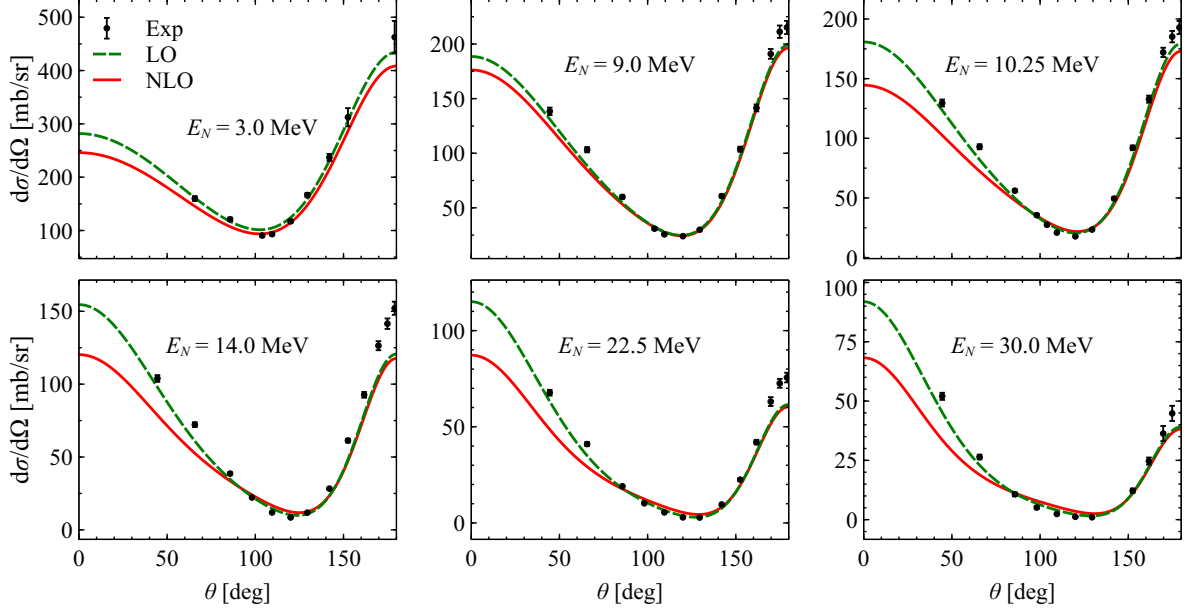


FIG. 6. The LO and NLO angular distributions at various E_N . The neutron-deuteron scattering data are from Ref. [44].

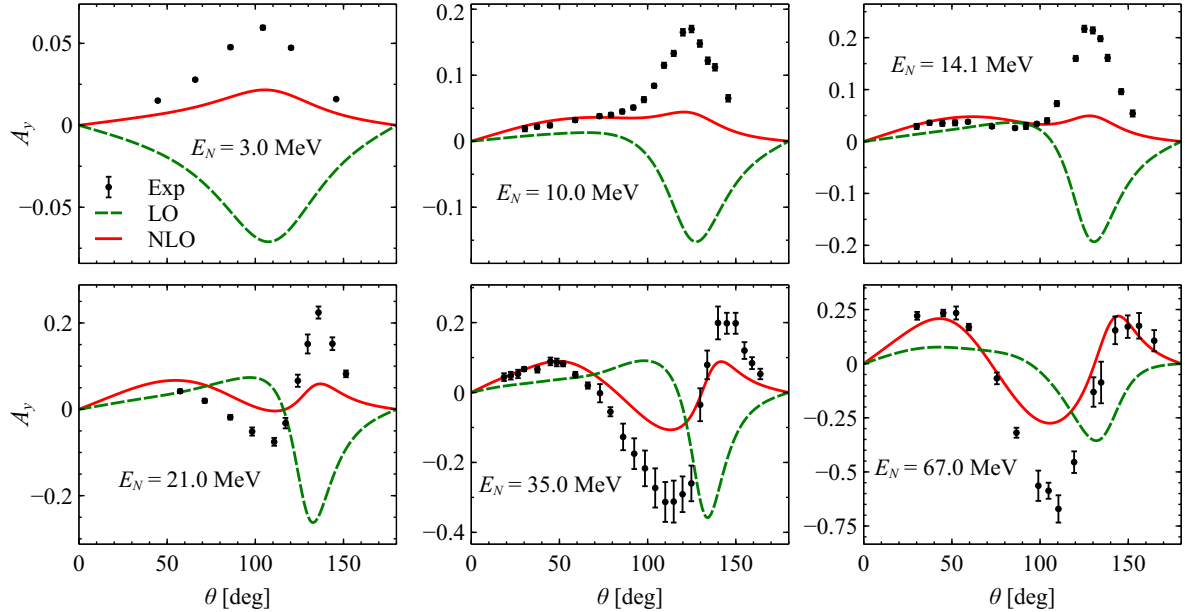


FIG. 7. The LO and NLO nucleon analyzing power at various E_N . The neutron-deuteron scattering data at $E_N = 3.0$, $E_N = 10.0$ and 14.1 , $E_N = 21.0$, and $E_N = 67.0$ MeV are from Refs. [45], [46], [47], and [48], respectively. The proton-deuteron data at $E_N = 35.0$ MeV are from Ref. [49].

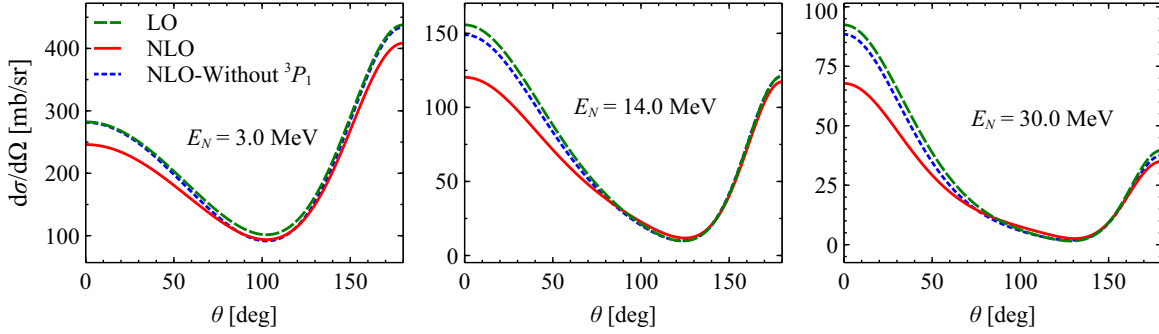


FIG. 8. The LO and NLO angular distributions at various E_N . Similar to Fig. 6, but the dotted curves are the NLO with the 3P_1 OPE turned off.

VI. SUMMARY

We have performed calculations of neutron-deuteron elastic scattering using renormalization-group-invariant chiral nuclear forces up to next-to-leading order, as developed in Refs. [16–18]. In our implementation of the Faddeev equation, a contour-deformation technique is employed, avoiding subtractions of the singularities of the integral equation. Strict perturbative calculations for the NLO potential after treating the LO nonperturbatively are performed. We demonstrated that computational costs can be substantially reduced in perturbation theory by leveraging the fact that the LO potentials are restricted to just a few NN partial waves. This approach yields a hierarchy of linear equations characterized by a fixed kernel — determined solely by the LO NN channels and their matrix elements — with driving terms that incorporate the higher-order potentials. The WPCD method was first used to benchmark our techniques. Good agreement was found for the phase shifts, elastic scattering differential cross sections, and nucleon analyzing powers.

We used these techniques to calculate the nd scattering phase shifts for the doublet and quadruplet S waves. The phase shifts were found to converge with respect to the cutoff Λ up to 1600 MeV. This finding is consistent with earlier work, where RG invariance of the triton binding energy and nd scattering lengths indicated that three-nucleon forces are not required for renormalization purposes up to NLO. In comparisons with experimental data, we found that although the NLO calculation underpredicts the differential cross section at forward angles relative to LO, it generally yields better agreement for the analyzing power A_y .

ACKNOWLEDGMENTS

We would like to thank Zeyuan Ye, Kaifei Ning, and Jinlong Dang for their contributions at early stages of developing the Faddeev code used in the paper. The work was supported by the National Natural Science Foundation of China (NSFC) under Grant Nos. 12275185, 12335002, and U2067205, and National Key R&D Program of China (No. 2023YFA1606702). DYP thanks O.A. Rubtsova for providing the codes for solveing the Faddeev equatiosn with the WPCD method.

[1] H. Witala, T. Cornelius, and W. Gloeckle, *Few-Body Syst.* **3**, 123–134 (1988).

[2] W. Glockle, H. Witala, D. Huber, H. Kamada, and J. Golak, *Phys. Rept.* **274**, 107 (1996).

[3] D. Hüber, W. Glöckle, J. Golak, H. Witała, H. Kamada, A. Kievsky, S. Rosati, and M. Viviani, *Phys. Rev. C* **51**, 1100 (1995).

[4] W. Gloeckle, T. Cornelius, and H. Witala, *Nucl. Phys. A* **508**, 115C (1990).

[5] H. Witala, H. Kamada, A. Nogga, W. Gloeckle, C. Elster, and D. Huber, *Phys. Rev. C* **59**, 3035 (1999), [arXiv:nucl-th/9901047](https://arxiv.org/abs/nucl-th/9901047).

[6] A. Kievsky, M. Viviani, and S. Rosati, *Phys. Rev. C* **56**, 2987 (1997), [arXiv:nucl-th/9706064](https://arxiv.org/abs/nucl-th/9706064).

[7] H. Witaa, A. Nogga, H. Kamada, W. Gloeckle, J. Golak, and R. Skibinski, *Phys. Rev. C* **68**, 034002 (2003).

[8] L. Girlanda, E. Filandri, A. Kievsky, L. E. Marcucci, and M. Viviani, *Phys. Rev. C* **107**, L061001 (2023), [arXiv:2302.03468 \[nucl-th\]](https://arxiv.org/abs/2302.03468).

[9] H. Witala, W. Gloeckle, J. Golak, H. Kamada, J. Kuros-Zolnierzuk, A. Nogga, and R. Skibinski, *Phys. Rev. C* **63**, 024007 (2001), [arXiv:nucl-th/0010013](https://arxiv.org/abs/nucl-th/0010013).

[10] S. B. S. Miller, A. Ekström, and K. Hebeler, *Phys. Rev. C* **106**, 024001 (2022), [arXiv:2201.09600 \[nucl-th\]](https://arxiv.org/abs/2201.09600).

[11] A. Margaryan, R. P. Springer, and J. Vanasse, *Phys. Rev. C* **93**, 054001 (2016), [arXiv:1512.03774 \[nucl-th\]](https://arxiv.org/abs/1512.03774).

[12] J. Golak *et al.*, *Eur. Phys. J. A* **50**, 177 (2014), [arXiv:1410.0756 \[nucl-th\]](https://arxiv.org/abs/1410.0756).

[13] H. Witala, J. Golak, R. Skibinski, and K. Topolnicki, *J. Phys. G* **41**, 094011 (2014), [arXiv:1310.0198 \[nucl-th\]](https://arxiv.org/abs/1310.0198).

[14] E. Epelbaum *et al.*, *Eur. Phys. J. A* **56**, 92 (2020), [arXiv:1907.03608 \[nucl-th\]](https://arxiv.org/abs/1907.03608).

[15] H. Witala, J. Golak, and R. Skibiński, *Phys. Rev. C* **105**, 054004 (2022), [arXiv:2203.08499 \[nucl-th\]](https://arxiv.org/abs/2203.08499).

[16] B. Long and C. J. Yang, *Phys. Rev. C* **85**, 034002 (2012), [arXiv:1111.3993 \[nucl-th\]](https://arxiv.org/abs/1111.3993).

[17] B. Long and C. J. Yang, *Phys. Rev. C* **86**, 024001 (2012), [arXiv:1202.4053 \[nucl-th\]](https://arxiv.org/abs/1202.4053).

[18] S. Wu and B. Long, *Phys. Rev. C* **99**, 024003 (2019), [arXiv:1807.04407 \[nucl-th\]](https://arxiv.org/abs/1807.04407).

- [19] W. Shi, R. Peng, T.-X. Liu, S. Lyu, and B. Long, *Phys. Rev. C* **106**, 015505 (2022), arXiv:2205.02000 [nucl-th].
- [20] T.-X. Liu, R. Peng, S. Lyu, and B. Long, *Phys. Rev. C* **106**, 055501 (2022), arXiv:2207.04241 [nucl-th].
- [21] A. J. Andis, S. Lyu, B. Long, and S. König, (2025), arXiv:2512.12823 [nucl-th].
- [22] O. Thim, A. Ekström, and C. Forssén, *Phys. Rev. C* **112**, 064008 (2025), arXiv:2510.12207 [nucl-th].
- [23] S. R. Beane, P. F. Bedaque, L. Childress, A. Kryjevski, J. McGuire, and U. van Kolck, *Phys. Rev. A* **64**, 042103 (2001), arXiv:quant-ph/0010073.
- [24] M. Pavon Valderrama and E. Ruiz Arriola, *Phys. Rev. C* **70**, 044006 (2004), arXiv:nucl-th/0405057.
- [25] A. Nogga, R. G. E. Timmermans, and U. van Kolck, *Phys. Rev. C* **72**, 054006 (2005), arXiv:nucl-th/0506005.
- [26] B. Long and U. van Kolck, *Annals Phys.* **323**, 1304 (2008), arXiv:0707.4325 [quant-ph].
- [27] S. Weinberg, *Phys. Lett. B* **251**, 288 (1990).
- [28] S. Weinberg, *Nucl. Phys. B* **363**, 3 (1991).
- [29] S. Weinberg, *Phys. Lett. B* **295**, 114 (1992), arXiv:hep-ph/9209257.
- [30] D. B. Kaplan, *Phys. Rev. C* **102**, 034004 (2020), arXiv:1905.07485 [nucl-th].
- [31] H. W. Hammer, S. König, and U. van Kolck, *Rev. Mod. Phys.* **92**, 025004 (2020), arXiv:1906.12122 [nucl-th].
- [32] J. Vanasse, *Phys. Rev. C* **88**, 044001 (2013).
- [33] R. G. Seyler, *Nucl. Phys. A* **124**, 253 (1969).
- [34] W. Glöckle, *The Quantum Mechanical Few-Body Problem* (Springer, Berlin, Heidelberg, 1983).
- [35] Y. K. Ho, *Phys. Rept.* **99**, 1 (1983).
- [36] N. Moiseyev, *Phys. Rept.* **302**, 212 (1998).
- [37] T. Myo, Y. Kikuchi, H. Masui, and K. Katō, *Prog. Part. Nucl. Phys.* **79**, 1 (2014), arXiv:1410.4356 [nucl-th].
- [38] T. Myo and K. Kato, *PTEP* **2020**, 12A101 (2020), arXiv:2007.12172 [nucl-th].
- [39] W. Glöckle, G. Hasberg, and A. R. Neghabian, *Z. Phys. A* **305**, 217 (1982).
- [40] V. Pomerantsev, V. Kukulin, O. Rubtsova, and S. Sakhiev, *Computer Physics Communications* **204**, 121 (2016).
- [41] S. B. S. Miller, A. Ekström, and C. Forssén, *J. Phys. G* **49**, 024001 (2022), arXiv:2106.00454 [nucl-th].
- [42] Q.-Y. Zhai, D.-Y. Pang, W.-D. Chen, O. A. Rubtsova, R.-R. Xu, J.-X. Lu, H. Liang, and L.-S. Geng, (2025), arXiv:2512.02475 [nucl-th].
- [43] Y.-H. Song, R. Lazauskas, and U. van Kolck, *Phys. Rev. C* **96**, 024002 (2017), [Erratum: *Phys. Rev. C* 100, 019901 (2019)], arXiv:1612.09090 [nucl-th].
- [44] P. Schwarz, H. Klages, P. Doll, B. Haesner, J. Wilczynski, B. Zeitnitz, and J. Kecskemeti, *Nuclear Physics A* **398**, 1 (1983).
- [45] J. E. McAninch, W. Haeberli, H. Witała, W. Glöckle, and J. Golak, *Phys. Lett. B* **307**, 13 (1993).
- [46] C. R. Howell, W. Tornow, K. Murphy, and et al., *Few-Body Systems* **2**, 19–32 (1987).

- [47] G. J. Weisel, W. Tornow, and J. H. Esterline, *J. Phys. G* **42**, 085106 (2015).
- [48] H. Rühl *et al.*, *Nucl. Phys. A* **524**, 377 (1991).
- [49] S. N. Bunker, J. M. Cameron, R. F. Carlson, J. R. Richardson, P. Tomaš, W. T. H. Van Oers, and J. W. Verba, *Nucl. Phys. A* **113**, 461 (1968).